*Article*

# Intelligent Identification and Prediction Mineral Resources Deposit Based on Deep Learning

**Le Gao [1], Kun Wang [2,*], Xin Zhang [1] and Chen Wang [1]**

[1] Faculty of intelligent manufacturing, Wuyi university, Jiangmen, 529000, China. Le.gao@nscc-gz.cn
[2] Institute of Mineral Resources, Chinese Academy of Geological Sciences, Beijing, 100037, China
* Correspondence: wangkun@cags.ac.cn

**Abstract:** In recent years, intelligent identification and prediction of ore deposits based on deep learning algorithm and image processing technology has gradually become one of the research frontiers in the field of geological and metallogenic prediction. However, this method also has many problems that need to be solved. For example, (1) very few trainable image samples containing mineral point labels; (2) The geological image features are small and irregular, and the image similarity is high; (3) It is difficult to calculate the influence of different geological prospecting factors on ore mineralization. Based on this, this paper constructs a deep learning network model Multiscale Feature Attention Framework (MFAF) based on geo-image data. The results show that MFCA-Net module in MFAF model can solve the problem of scarce mine label images to a certain extent. In addition, the channel attention mechanism SE-Net module can quantify the difference of influence of different source factors on mineralization. The prediction map is obtained by applying the MFAF model in the study of deposit identification and prediction in the research area of the southern section of Qin-hang metallogenic Belt. In the forecast map, many regions have high metallogenic potential. Through observation, it is found that the above predicted area covers 100% of the known ore deposits at present, which has a good prediction effect. Later, we can find out the specific reasons through field verification. The multi-scale feature fusion and attention mechanism MFA Framework in this paper can provide a new way of thinking for geologists in mineral exploration. The research of this paper also provides resource guarantee and technical support for the sustainable exploitation of mineral resources and the sustainable growth of society and economy.

**Keywords:** Artificial Intelligence; Sustainable development; Deep Learning; Mineral Deposit Prediction; Multi-scale Features; Attention Mechanism

## 1. Introduction

Mineral resources are an important resource guarantee for sustainable economic growth and stable social development. With the continuous exploitation and consumption of mineral deposits, many precious resources are facing the risk of scarcity. So geologists began to explore new techniques and methods to find new deposits. In recent years, with the development of artificial intelligence and big data technology in geology, intelligent prediction of mineral resources based on machine learning algorithm and image processing technology has gradually become one of the frontier hot spots for geologists and scientific researchers [1-3]. Many scholars use Logistic Regression [4], Support Vector Machine(SVM) [5], Genetic algorithm [6], Random forest Forest(RF) [7], Artificial Neural Network(ANN) [8] and other artificial intelligence algorithms have carried out intelligent prediction and mineral analysis of geological and mineral resources. It is proved that machine learning and deep learning algorithms have strong prediction ability in identifying the nonlinear relationship between ore deposits and metallogenic conditions, and can significantly improve the accuracy and success rate of prediction. For example, Zuo and Carranza [9] used SVM algorithm to predict the Nova Scotia gold deposit in western Canada, which confirmed that SVM algorithm has obvious advantages in prediction accuracy and precision compared with traditional weight of evidence method. Daviran et al. [10] used genetic algorithm to optimize the super parameters of random forest to improve the

Preprints (www.preprints.org) | NOT PEER-REVIEWED | Posted: 5 June 2023 doi:10.20944/preprints202306.0285.v1

accuracy of mine target prediction. Chen et al. [11] proposed a novel ensemble scheme for MPM using wavelet neural network (WNN) and Monte Carlo simulation (MCs) to address the forementioned issues. The resulting predictive map provides important clues of W-Sn deposit occurrences which could stimulate future mineral exploration in the Nanling Range. Marjanovic et al. [12] adopted Convolutional Neural Network (CNN), Recurrent Neural Network (RNN) and Multilayer Perceptron (MLP) and Random Forest (RF) machine learning algorithms analyzed mineral composition data from 488 sediment samples. The results show that trained machine learning models can help experts analyze mineral composition more efficiently and reliably.

As a deep artificial intelligence image algorithm, deep learning has been actively applied in geological information metallogenic prediction and achieved many innovative results [13-18]. In previous studies, some scholars use CNN methods [19], Deep Convolutional Neural Network (DCNN) [20] and Long Short-Term Memory Network (LSTMN) [21], Generative Adversarial Network (GAN) [22] and Transfer Learning (TL) [23] and other deep learning algorithms have carried out intelligent prediction of geochemical mineral resources, proving that deep learning algorithm is a powerful tool for geochemical element concentration analysis and metallogenic prediction. For example, Chen and Shayilan [24] used deep learning technology to establish a learning model for multi-geochemical anomaly detection oriented to prospecting targets. The test results show that the model algorithm is worthy of further study in the field of prospecting with complex geochemical background. He et al. [25] made a review of the research of machine learning in the field of geochemistry, and the research results predicted that deep learning and machine learning technology would achieve great breakthroughs in the research of geochemistry. Huang et al. [26] used the deep learning method to capture the characteristics of geochemical elements and build a deep intelligent prospecting target prediction framework. The experimental results show that the multi-scale feature deep learning framework has significant advantages compared with other deep learning methods.

However, deep learning technology is still in the exploratory stage in mining and forecasting geological prospecting information, and there are still some problems to be solved. Common problems include: (1) Due to the scarcity of mineral points in the study area, trainable image samples containing mineral point labels are very few; (2) Due to the fine and irregular features of geological images, the image similarity is high and it is difficult to extract effective information; (3) The degree of influence of geological prospecting factors of different data sources on ore mineralization. All these problems bring more challenges and opportunities for geological workers in ore deposit prediction. Based on the above problems, this paper takes the Jinshan research area in the southern section of the Qinhang metallogenic Belt of China as the research object, takes the drainage sediment geochemical data and mineral geological map as the basic data sources, and constructs the deep learning network model based on the geological image data. This research proposes a deep learning model of Multiscale Feature Attention Framework (MFAF). The framework of MFAF research is shown in Figure 1. It mainly consists of two parts: MFCA-Net (Multiscale feature channel attention Net) and CSA-Net(Convolution spatial attention Net). MFCA-Net uses the set of expansion coefficients $\alpha$={$\alpha$1, $\alpha$2, $\alpha$3…$\alpha$n}and the channel attention mechanism Squeeze- and - Excitation Block (SE-Net) module. The framework consists of three steps: (1) The expansion coefficient set $\alpha$ is used to generate convolution kernels of different scales, and the feature maps of different scales are obtained to solve the question of a small number of known deposits in the study area, and to provide data support for the convolution operation to extract more and more detailed feature information in this area. (2) The feature image generated after expansion convolution will pass through the channel attention module, which comprises both compression and excitation processes. In the compression stage, the global compression feature quantity is obtained by global pooling on the feature graph. At the bottleneck phase, the weights of each channel in the Feature Map are obtained through a bottleneck structure that is fully connected at two layers, and the weighted Feature Map is used as input to the next layer network. Therefore, the extracted features are re-calibrated, and different weight values are assigned to the features in different channels $W = \{W_1, W_2, \ldots, W_n\}$, , so as to solve the problem that different geochemical elements have different influence degrees on mineralization (3) The CSA-Net module mainly includes a series of convolution operations. Considering that the element content of different spatial locations in the feature map has different influences on mineralization, the last layer of

Preprints (www.preprints.org) | NOT PEER-REVIEWED | Posted: 5 June 2023 doi:10.20944/preprints202306.0285.v1

convolution is added with the spatial attention module to assign different weight coefficients to the features of different locations. In order to reduce the number of training parameters and accelerate the model convergence, each channel was finally classified by the shared full connection layer.

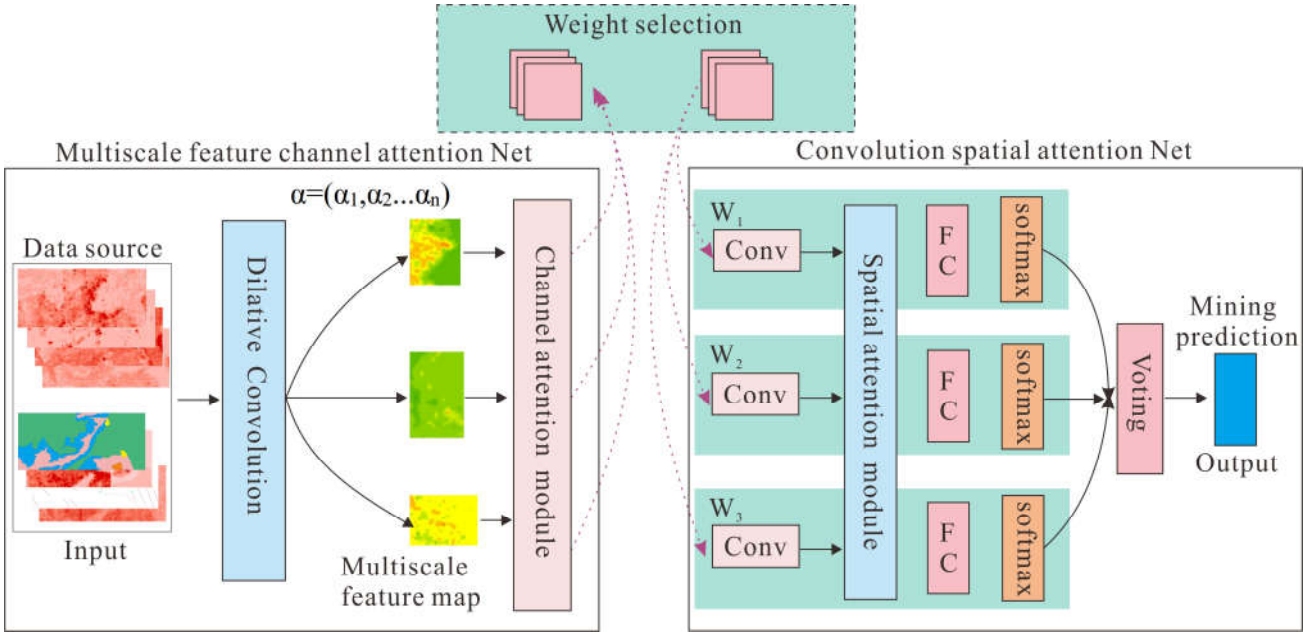


**Figure 1.** Multiscale Feature Attention Framework.

## 2. Study Area and Materials

The study area Jinshan is located in the southern section of China's Qin-hang (Qinzhou Bay - Hangzhou Bay) metallogenic belt, which is a giant structural junction belt located in the middle of two ancient landmass of Yangtze and Huaysia. The belt extends from Hangzhou Bay in the northeast to Qinzhou Bay in the southwest with a total length of 2000km and has good metallogenic potential. Figure 2 shows a general map of geology and mineral resources in the study area. Red dots are known deposit locations, and blue dots are stream sediment sampling locations. There are five major strata in the study area: Triassic, Permian, Carboniferous, Devonian, and Quaternary. Among them, the Triassic lithologic is given priority to gray, gray, sandy mudstone, lower than white, thin layer and so tuffaceous shale. Permian lithology is light gray thick - bedded bioclastic limestone, sand-clastic limestone and microcrystalline limestone. The Carboniferous lithology is composed of gray middle-thick bedded bioclastic limestone, gray white thick bedded dolomite and biooritic microcrystalline limestone. Devonian lithology is dark gray thin bedded limestone, microcrystalline limestone, marbled limestone. The structural development in this area is dominated by faults, including regional major faults, NE trending faults, NW faults, near - south - north faults and interlayer fracture zones. Regional metallogenic influenced by lithology and tectonic common control, the ore formation of Triassic, known ore deposits are situated near the faults and fissures, obviously controlled by fracture structure. The data sources analyzed in this study include mineral geological maps and stream sediment geochemical element data. According to statistics, we sampled 3568, 1559, 1942, 342, and 101 samples from each formation, for a total of 7512 samples. The data analyzed by stream sediment

Preprints (www.preprints.org) | NOT PEER-REVIEWED | Posted: 5 June 2023 doi:10.20944/preprints202306.0285.v1

survey include Ag, Au、B、Sn、Cu、Ba、Mn、Pb、Zn、As、Sb、Hg、Mo、W、Bi and F. Table 1 shows part of the geochemical element data, X and Y correspond to sampling point coordinates.

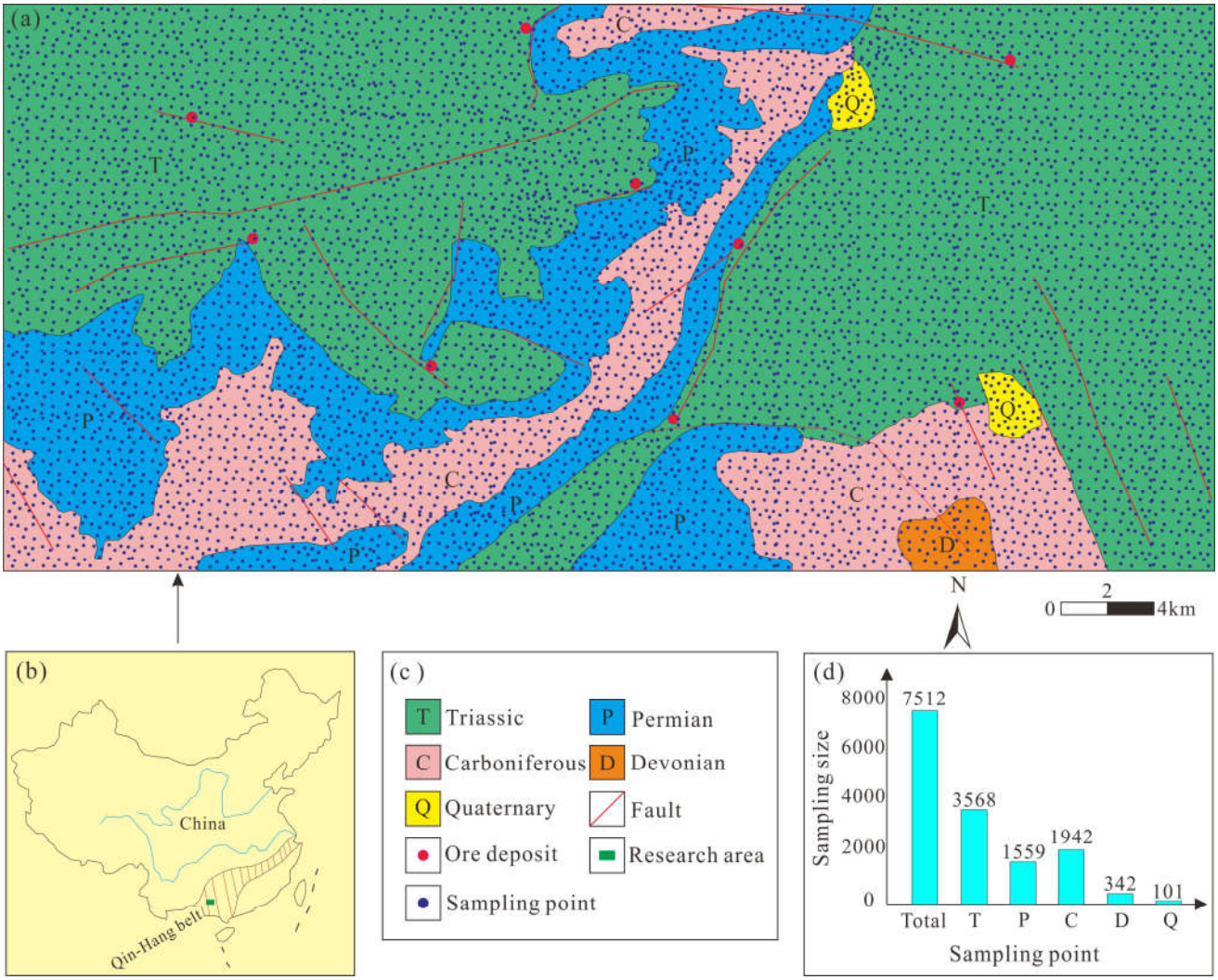


**Figure 2.** Geological Map of the Study Area. (a Geological map, b Location of the study area, c Legend, d Sampling quantity)

**Table 1.** Geochemical Element Data Set (The unit of Au and Ag are ng/g, other element unit is μg/g).

| X | Y | Ag | Au | B | Sn | Cu | Ba | Mn | Pb | Zn | As | Sb | Hg | Mo | W | Bi | F |
|---|---|---|---|---|---|---|---|---|---|---|---|---|---|---|---|---|---|
| 421.63 | 2416.85 | 0.078 | 0.54 | 4 | 2.56 | 7 | 88 | 209 | 12 | 23 | 0.9 | 0.29 | 0.04 | 0.82 | 1.16 | 0.42 | 204 |
| 420.93 | 2416.80 | 0.06 | 0.81 | 3 | 3.74 | 5 | 885 | 305 | 33 | 22 | 0.58 | 0.36 | 0.04 | 0.82 | 1.11 | 1.41 | 222 |
| 420.95 | 2416.35 | 0.086 | 0.94 | 4 | 2.41 | 5 | 797 | 267 | 53 | 35 | 1.15 | 0.34 | 0.09 | 0.51 | 1.16 | 0.42 | 212 |
| 421.21 | 2415.85 | 0.043 | 0.81 | 3 | 1.52 | 5 | 1111 | 423 | 42 | 14 | 0.51 | 0.35 | 0.07 | 0.59 | 0.38 | 0.23 | 222 |
| 420.30 | 2416.35 | 0.046 | 0.37 | 2 | 1.65 | 6 | 941 | 498 | 38 | 17 | 0.53 | 0.31 | 0.02 | 0.57 | 0.33 | 0.61 | 222 |
| 419.86 | 2416.15 | 0.033 | 1.09 | 4 | 1.53 | 8 | 427 | 338 | 37 | 29 | 0.74 | 0.28 | 0.07 | 1.68 | 0.73 | 0.47 | 204 |

Preprints (www.preprints.org) | NOT PEER-REVIEWED | Posted: 5 June 2023 doi:10.20944/preprints202306.0285.v1

## 3. Methods

### *3.1 Multi-scale feature fusion*

With the deepening of the number of layers in the deep learning network, the semantic expression ability is enhanced, but this also reduces the resolution of the image, and many detailed features become more and more fuzzy after the convolution operation of the multi-layer network. The traditional target detection model results in the reduction of the effective information of small targets on the last feature map. Multi-scale feature fusion is a good solution to this question. Instead of using the feature map of the last layer for detection, multi-layer features are selected for fusion and then detection, so as to obtain images of multiple scales, and then the classification algorithm is adopted to realize the task of image classification [27, 28]. The multi-scale feature fusion diagram is shown in Figure 3. At present, a large number of researchers in the field of artificial intelligence have carried out a lot of research on multi-scale feature fusion and image recognition technology [29-31], and achieved good results. In recent years, some geological experts have applied multi-scale feature fusion technology to geological prospecting and geochemical analysis, and achieved fruitful results. For example, Guan et al. [32] proposes a feature fusion convolutional autoencoder to extract and fuse the spatial structural features and compositional relationships of multivariate geochemicals for identifying geochemical anomalies. The results shows the method are applicable and reliable for mineral resource exploration. Zhou et al. [33] combined multi-scale geophysical prospecting technology with geological prospecting in typical deposit areas to provide evidence for geologists to understand the metallogenic background and discover new deposits. Li et al. [34] presents a multi-modal feature fusion based framework to improve the geographic image annotation. The comprehensive experiments show that this feature fusion based method achieves much better performances compared to traditional methods.

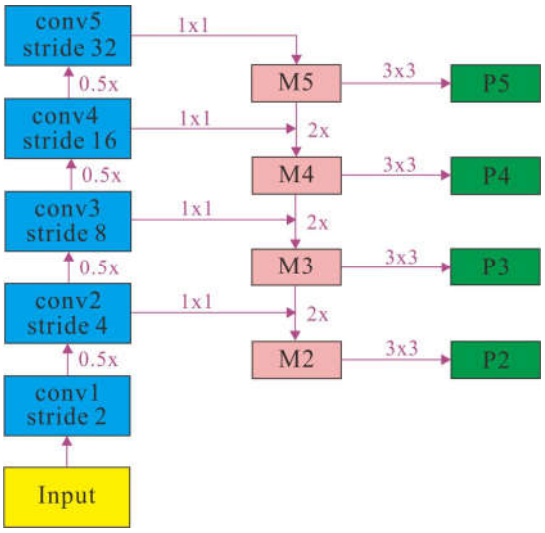


**Figure 3.** Multi-Scale Feature Fusion Flow Chart.

In order to solve the problem of few mineral points and few ore-bearing label images in the study area, geological layers, fracture images and a variety of geochemical elements can be used to generate geological image data of different scales, and image data sets can be generated by unsynchronously long sliding Windows to increase the diversity of data samples. For the input geological data bases set $x' = \{x_i\}_{i=1}^{N}$, the expansion coefficient set $\alpha$={$\alpha$1, $\alpha$2, $\alpha$3... $\alpha$n} generates convolution of different sizes to check the convolution operation, and generates the image of multi-scale features. Specifically, we use the convolution operation of the convolution kernel $M = \{M_1, M_2, \ldots, M_n\}$ and the set $\alpha$ of expansion coefficients to obtain the multi-scale feature graph F={F1,F2... ,Fn}, where the ith feature is $F_i$. The specific generation formula 1 is shown as follows: where xi represents the ith feature element, Mi represents the convolution weight corresponding to

Preprints (www.preprints.org) | NOT PEER-REVIEWED | Posted: 5 June 2023 doi:10.20944/preprints202306.0285.v1

the generation of the ith feature graph, $\alpha$i represents the expansion convolution coefficient corresponding to the generation of the ith feature graph, and r represents the convolution channel.

$$F_i = r(x_i, M_i, \alpha_i) \quad (1)$$

*3.2 Channel Attention*

In the research of deep learning algorithms, Channel Attention (CA) mechanism is a resource allocation mechanism, which can make the model training of neural network focus on the important features of the image and improve the efficiency and accuracy of the neural network. Each channel of a feature map is a feature detector, and the channel attention mechanism pays different attention to different image channels [35]. At present, many scholars have conducted in-depth studies on the mechanism of attention, and achieved good results [36-38]. Some earth science experts have combined the channel attention mechanism with geoscience images, and the image classification effect has been significantly improved. For example, Zhu et al. [39] proposed super-resolution model employs residual channel attention networks as a backbone structure. The experimental results confirmed that the enhanced multi-temporal images can bring substantial improvement on classification. Gajbhiye et al. [40] combined the channel attention mechanism and convolutional neural network to generate letters for remote sensing images, and conducted model evaluation in the test set, and obtained good results. The channel attention module is shown in Figure 4. For image input features, firstly, the maximum pooling and average pooling algorithms are used simultaneously, then transformation results are obtained through several Multilayer perceptron and MLP layers, and finally the transformation results are respectively applied to the two channels, so that the sigmoid function can obtain the attention results of the channels. The calculation procedure is shown in Formula 2. In Formula 2, Mc is the channel attention result, F is the input feature, σ is the sigmoid function, MLP is the Multilayer perceptron, AvgPool is the average pooling, and MaxPool is the maximum pooling.

$$Mc = \sigma(\mathrm{MLP}(\mathrm{AvgPool}(F) + \mathrm{MaxPool}(F))) \quad (2)$$

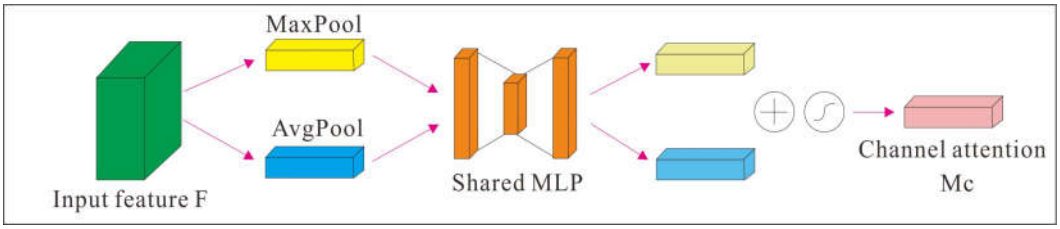


**Figure 1.** Channel Attention Module.

In this paper, mineral geological image and geochemical element image are used to study the identification and prediction of ore deposits. Different data sources contain a variety of geological prospecting factors, and different geological prospecting factors have different degrees of influence on ore deposits. Therefore, in order to reduce the influence of human factors, this study adopted channel attention module in the process of training data. According to the value of loss in the experiment, the weight values on different channels are adjusted reversely and dynamically, the weight values of important features are increased, the importance of features with little influence is suppressed, and the representational power of our network training model is improved. By assigning the optimal weight value to each channel, the convergence of the network model is accelerated and the accuracy of the deposit prospecting prediction is improved.

*3.3 Spatial Attention*

In the study of using artificial intelligence technology to analyze image data, different areas in the image have different contribution degrees to the task, and only the areas related to the task are the ones we need to pay the most attention to. Spatial attention(SA) can be regarded as an adaptive spatial region selection mechanism: where to focus [41]. At present, many scholars have integrated spatial attention module into deep learning network model to improve the training effect of the

Preprints (www.preprints.org) | NOT PEER-REVIEWED | Posted: 5 June 2023 doi:10.20944/preprints202306.0285.v1

model [42-44]. Some geological experts focus on the spatial distribution of geological images and data, and achieve good results in image modeling and image classification. For example, Pan et al. [45] proposed an integrated method to effectively integrate multi-source complex spatial data, which combined spatial model with complex stratigraphic modeling technology to realize the visualization of spatial model. Zhao and Wang [46] used the machine learning method to analyze the spatial distribution of geochemical elements such As Au, As, Sb and Hg. The results show that the geochemical anomalies extracted by this method are consistent with the known metallogenic areas, which proves that this method is feasible and effective in identifying geochemical anomalies. In the spatial attention module of Figure 5, we firstly reduce the dimension of the channel itself, obtain the results of maximum pooling and mean pooling respectively, and then assemble them into a feature map, and then use a convolution layer for learning. The calculation procedure is shown in Formula 3. In formula 3, Ms is spatial attention as a result, F for the input characteristics, σ as sigmoid function, $f^{7*7}$ is 7 x 7 size of convolution kernels, AvgPool for average pooling, MaxPool for maximum pool.

$$Ms = \sigma( f^{7*7} ( AvgPool( F); MaxPool( F))) \quad (3)$$

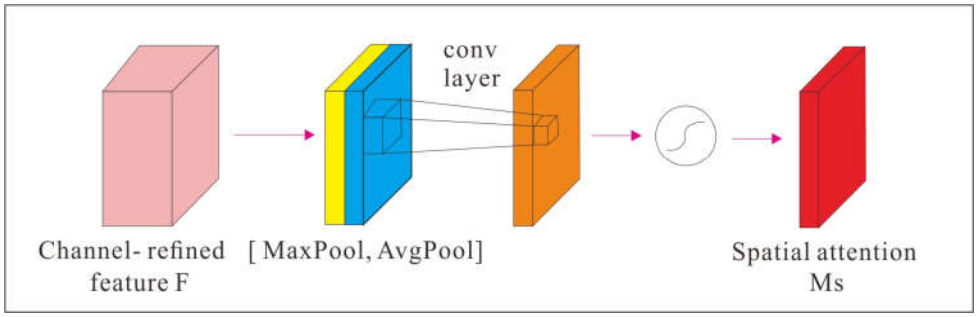


**Figure 2.** Spatial Attention Module.

In this paper, considering the difference of geological prospecting factors in different spatial locations on mineralization of ore deposits, spatial attention module is adopted in the model. The spatial attention module can use spatial attention as a supplement to the convolution operation, which enhances or supposes image features at different spatial locations.

### *3.4. Fully Connected Layer, Softmax and Voting*

In the CNN structure, after image data passes through multiple convolution layers and pooling layers,one or more Fully Connected layers (FC) are connected, and each neuron in the Fully Connected layer is fully connected with all the neurons in the previous layer. It can integrate different types of information in the convolution layer and the pooling layer. In order to improve the performance of CNN network, the excitation function of each neuron in the fully connected layer generally adopts ReLu function [47]. After passing through the fully connected layer, we used softmax to classify the image data, and used the voting mechanism to predict and classify the positions with and without ore in the study area. Through the above steps, we could improve the overall prediction accuracy of the network model.

In this paper, the characteristics of input geological prospecting factors $X = \{x_i\}_{i=1}^{N}$ through expansion convolution of different coefficients can obtain the set $F = \{F_1, F_2, F_3, \ldots F_k\}$ of its feature map, where $F_i = \{F_j^i\}_{j=1}^{N}$. Our network model firstly extracts features from set F, then performs global pooling operations, allocates different weights to different positions through the spatial attention module, and finally obtains its output results through the fully connected layer. The optimal cross entropy method was adopted to optimize the network structure of the classification model, as shown in Formula 4. In Formula 4, $\partial^i$ is the weight parameter in SACNet, yi is the label value of the i geological prospecting factor feature, and loss(*) is the calculation of cross entropy loss after Softmax is activated.

$$L = \sum_{i=1}^{M} \sum_{j=1}^{N} loss(\partial^i; P_j^i; y_i) \quad (4)$$

After the above calculation, we vote on the probability distribution calculated by softmax for each channel network and obtain the final prediction result. The probability distribution after using

Preprints (www.preprints.org) | NOT PEER-REVIEWED | Posted: 5 June 2023 doi:10.20944/preprints202306.0285.v1

softmax is, $P = \{P_i\}_{i=1}^{k}, P_i = [P_0, P_1]$ , where $P_0$ is the probability predicted to be "ore free" and $P_1$ is the probability predicted to be "ore present". We obtain the prediction results of each channel network through formula 5, and determine the final prediction results through the vote of formula 6.

$$\hat{y}_i = \text{argmax}(P_i) \quad (5)$$

$$\hat{y} = \text{vote}(\{\hat{y}_i\}_{i=1}^{k}) \quad (6)$$

## 4. Results and discussion

### *4.1. Data pre-processing*

In this study, the preprocessing of the original geological data is divided into four steps.

(1) Screen out favorable geochemical elements for mineralization. In this study, the support vector model was used to obtain the Area Under Curve(AUC) value of each element, and the ZAUC value was calculated by the formula (7-9) :

$$Q_1 = \frac{AUC}{2 - AUC}, \quad Q_2 = \frac{2\,AUC^{\,2}}{1 + AUC} \quad (7)$$

$$S_{AUC} = \sqrt{\frac{AUC\,(1-AUC) + (C_p - 1)(Q_1 - AUC^2) + (C_n - 1)(Q_2 - AUC^2)}{C_p \times C_n}} \quad (8)$$

$$Z_{AUC} = \frac{AUC - 0.5}{S_{AUC}} \quad (9)$$

The random variable ZAUC meets the standard normal distribution, and the critical value is obtained by comparing the standard normal distribution table, which is used to detect whether there is a significant difference between AUC and 0.5. The results are shown in Table 2. When ZAUC value is greater than 0.01, the critical value of 2.58 is selected, that is, Ag, Au, Sn, Cu, Ba, Sb, Hg and Mo are selected as favorable prospecting factors.

**Table 2.** The results of AUC and ZAUC

| Element | AUC | ZAUC | Element | AUC | ZAUC |
|---|---|---|---|---|---|
| Au | 0.6024 | 2.8395 | B | 0.5901 | 2.4839 |
| Sn | 0.6065 | 2.9595 | Cu | 0.6311 | 3.6977 |
| Ag | 0.6762 | 5.1563 | Ba | 0.6147 | 3.2020 |
| Mn | 0.5573 | 1.5617 | Pb | 0.5778 | 2.1341 |
| Zn | 0.5450 | 1.2232 | As | 0.5655 | 1.7893 |
| Sb | 0.5942 | 2.6017 | Bi | 0.5901 | 2.4839 |
| Hg | 0.6393 | 3.9516 | Mo | 0.5983 | 2.7203 |
| W | 0.5778 | 2.1341 | F | 0.5696 | 1.9037 |

(2) The inverse distance weight method was used to interpolate the above 8 geochemical element data sets, and the corresponding element concentration contour map was obtained. This interpolation calculation experiment reference [48], the experimental results generated T grid points of element concentration map, where W is the width of the image, H is the height, T is the number of element distribution map. The calculation formula of the inverse distance weighting method is shown in (10) and (11) : where, is the Euclidean distance from the discrete point (xi, yi) to the grid point (x0, y0), is the valuation of the position, is the observed value at the discrete point i, and N is the number of discrete points involved in the calculation. In this study, the inverse distance weight method was applied to Ag, Au, Sn, Cu, Ba, Sb, Hg, Mo and other elements to generate 8 isoline maps of element concentration with the size of 1560×1560. Finally, the isoline map of element concentration, the geological layer and the fault structure layer were superimposed with the known ore deposit layer respectively to generate 10 new images of geological prospecting factors, as shown in Figure 6.

$$D_i = \sqrt{(x_0 - x_i)^2 + (y_0 - y_i)^2} \quad (10)$$

$$Z(x_0, y_0) = \sum_{i=1}^{N} \frac{1}{(D_i)^2} Z_i \Big/ \sum_{i=1}^{N} \frac{1}{(D_i)^2} \quad (11)$$

Preprints (www.preprints.org) | NOT PEER-REVIEWED | Posted: 5 June 2023 doi:10.20944/preprints202306.0285.v1

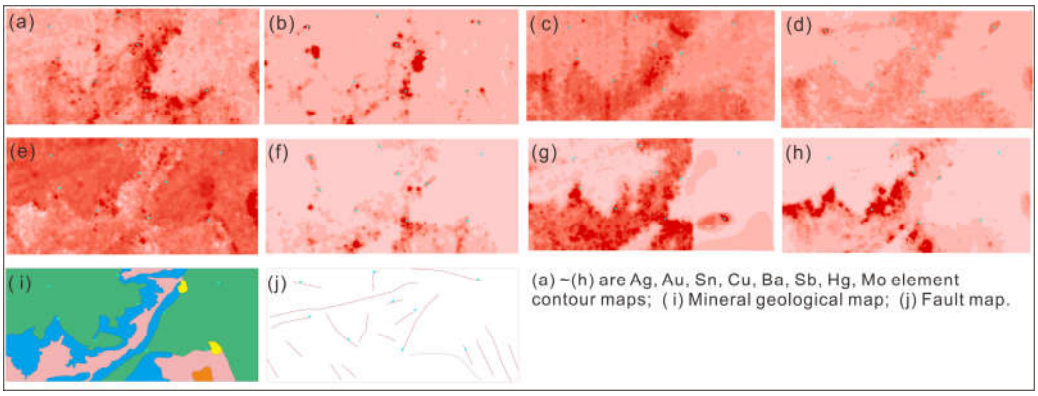


**Figure 6.** Geographic images.

(3) This step further processes the geoimage generated in Step 2 to obtain the geoimage data set. Firstly, a sliding window is defined, and the element content of each sampling point is obtained by sliding the geographic image with appropriate step size. After many experiments, the geographic image data set required by the cost research is generated. It is assumed that the geo-information training set is, which contains N samples, are various characteristic elements in it, and are their corresponding real labels. C is the number of geological information channels, where 0 represents "no ore" data and 1 represents "ore" data. In this experiment, 128×128 Windows and 128 pixels were used for sliding operation on the geo-information map to generate the geo-image data set needed for the final model training. This image data set includes 428 128×128×10 image data, among which 342 data are included in the training set, including 56 "ore" data and 286 "no ore" data. The test set contains 86 data, including 14 "ore" data and 72 "no ore" data.

(4) Extend the number of geological images generated in the previous step with Smote. In order to effectively train the deep learning network model, this experiment enhanced the image data by adding Gaussian noise with an average value of 0 and a variance of 0.01. In this paper, according to smote algorithm [49] and SMOTE method [50], give sample extension to the original geoscience image data set, and enhance the completeness of deep learning training model. Through this step, the final generated data set includes 654 128×128×10 data, among which 524 data are generated in the training set, including 224 "ore" data and 300 "no ore" data. The test set has 130 data, including 56 "ore" data and 74 "no ore" data. After data pre-processing in these four steps, the geoimage data set generated can be used as the input data of the MFAF in this study.

### *4.2. MFA Experiment*

The evaluation indexes of the model in this paper are accuracy, recall rate, AUC value, and F1-Score. All experiments are programmed and implemented with the Pytorch framework and one GeForce RTX 3090 GPU. In this experiment, ResNet18 [51] and ShuffleNetV2 [52] were used as the basic network, MFAF was adopted to optimize it, and the comparison experiment was conducted with the mainstream deep learning model. We used an SGD optimizer to iterate the experimental model with momentum of 0.2, weight decay of 1e-4, cycle iteration of 220 times, initial learning rate set at 0.02, decay of 40% every 30 times, and batch size of 32. In this paper, MFAF uses $\alpha$={$\alpha$1, $\alpha$2, $\alpha$3…$\alpha$n} MFI Framework [15] expansion coefficient is set to $\alpha$={1,6,12,18,24}.

The experimental results of different methods are shown in Table 3. We compared the following methods, including ResNet18 [51], ShuffleNetV2 [52], GoogLeNet [53], MobileNet [54] and MnasNet [55]. Compared with the unoptimized ResNet18 model, the performance of the optimized ResNet18 model has been greatly improved, with the Accuracy increased by 7.82%, the AUC value increased by 10.33%, the Recall rate increased by 10.61% and the F1-Score v,alue increased by 4.30%. Compared with the unoptimized ShuffleNetV2, the optimized ShuffleNetV2 model also has a great improvement in performance, with the accuracy rate increased by 4.86%, AUC value increased by 3.99%, recall rate increased by 18.89%, and F1-Score increased by 9.74%. The experimental results prove that MFA-Framework has good generalization and has certain advantages compared with

Preprints (www.preprints.org) | NOT PEER-REVIEWED | Posted: 5 June 2023 doi:10.20944/preprints202306.0285.v1

current popular frameworks. Especially after using MFAF to optimize ResNet18, both AUC and recall rate increased by more than 10%.

**Table 2.** Experimental Results of Different Methods.

| Methods | Accuracy | AUC | Recall | F1-Score |
|---|---|---|---|---|
| ResNet18[51] | 64.84 | 63.13 | 32.05 | 59.41 |
| ResNet18* | 72.66 | 73.46 | 42.66 | 63.71 |
| ShuffleNetV2[52] | 62.37 | 61.43 | 18.43 | 53.98 |
| ShuffleNetV2* | 67.23 | 65.42 | 37.32 | 63.72 |
| GoogLeNet[53] | 62.38 | 61.45 | 20.14 | 56.33 |
| MobileNetV2[54] | 64.23 | 64.13 | 16.23 | 58.36 |
| MnasNet[55] | 68.79 | 67.23 | 17.69 | 60.86 |

### *4.3. Channel Attention Module Experiment*

In order to explore the role of channel attention module in this MFAF, this section tests experiments without channel attention module in ResNet18* and ShuffleNetV2* methods respectively. We define No-CA-ResNet18* and No-CA-ShuffleNetV2 * for the non-use channel attention module. The experimental results are shown in Table 4. Compared with ResNet18* and No-CA-ResNet18*, the accuracy increased by 3.12%, the AUC value increased by 8.57%, the Recall increased by 8.68%, and the F1-Score increased by 5.07% after the channel attention module was used. Compared with ShuffleNetV2* and No-CA-ShuffleNetV2* , the accuracy increased by 3.81%, the AUC value increased by 2.18%, the Recall increased by 1.81%, and the F1-Score increased by 2.73%. The comparison results of the two groups showed that the overall indicators were improved after the channel attention module was used in MFAF, and the model effect was more ideal.

**Table 3.** Experimental Results of Channel Attention Module.

| Methods | Accuracy | AUC | Recall | F1-Score |
|---|---|---|---|---|
| ResNet18* | 72.66 | 73.46 | 42.66 | 63.71 |
| No-CA-ResNet18* | 69.54 | 64.89 | 33.98 | 58.64 |
| ShuffleNetV2* | 67.23 | 65.42 | 37.32 | 63.72 |
| No-CA-ShuffleNetV2* | 63.42 | 63.24 | 35.51 | 60.99 |

### *4.4. Spatial Attention Module Experiment*

In order to explore the role of spatial attention module in this paper's MFAF, this section tests experiments without using spatial attention module in ResNet18* and ShuffleNetV2* methods respectively. We define No-CA-ResNet18 * and No-CA-ShuffleNetV2* for not using spatial attention modules. The experimental results are shown in Table 5. Compared with ResNet18* and No-CA-ResNet18*, the accuracy increased by 1.53%, the AUC value increased by 1.78%, the Recall increased by 3.20%, and the F1-Score increased by 2.37% after the spatial attention module was used. Compared with ShuffleNetV2* and No-CA-ShuffleNetV2*, the accuracy increased by 2.75%, the AUC value increased by 1.46%, the Recall increased by 2.2%, and the F1-Score increased by 1.68%. The comparison results of the two groups showed that the overall indicators were improved after the spatial attention module was used in MFAF, and the model effect was more ideal.

**Table 4.** Experimental Results of Spatial Attention Module.

| Methods | Accuracy | AUC | Recall | F1-Score |
|---|---|---|---|---|
| ResNet18* | 72.66 | 73.46 | 42.66 | 63.71 |
| No-SA-ResNet18* | 71.13 | 71.68 | 39.46 | 61.34 |
| ShuffleNetV2* | 67.23 | 65.42 | 37.32 | 63.72 |
| No-SA-ShuffleNetV2* | 64.48 | 63.96 | 35.12 | 62.04 |

Preprints (www.preprints.org) | NOT PEER-REVIEWED | Posted: 5 June 2023 doi:10.20944/preprints202306.0285.v1

*4.5. Parameter Sensitivity Analysis Experiment*

The setting of Loss function and dilation rate will exert certain influence on the effect of deep learning network [56, 57]. This section mainly discusses the influence of loss function coefficient and expansion coefficient on the MFAF. Firstly, the influence of the setting of loss function coefficient on our research framework was discussed. In this experiment, the auxiliary loss function coefficient was set as 6 groups of comparison experiments, in which the loss function coefficient was set as {0, 0.1, 0.4, 0.6, 0.7, 0.8}. Based on the ResNet18 network structure, we conducted MFA network optimization experiment and obtained the comparison results. Table 6 shows the experiment results with different auxiliary loss function coefficients. As can be seen from Table 6, when the coefficient of loss function is 0, it means the original result of ResNet18. When the coefficient of the auxiliary loss function is 0.4, the output of the network architecture is the best. When the coefficients are set to 0.6, 0.7 and 0.8, the output results of the network architecture gradually deteriorate with the increase of the coefficients. Our auxiliary loss function coefficient is set to 0.4.

**Table 5.** Comparison of Experimental Results of Different Auxiliary Loss Functions.

| Loss function | Accuracy | AUC | Recall | F1-Score |
|---|---|---|---|---|
| 0 | 64.84 | 63.13 | 32.05 | 59.41 |
| 0.1 | 71.21 | 70.22 | 39.12 | 60.34 |
| 0.4* | 72.66 | 73.46 | 42.66 | 63.71 |
| 0.6 | 71.45 | 70.32 | 38.49 | 60.19 |
| 0.7 | 68.44 | 65.54 | 37.55 | 58.84 |
| 0.8 | 64.96 | 63.27 | 32.64 | 60.34 |

After the discussion of the coefficient of loss function, we continue to discuss the influence of the coefficient of expansion on the proposed MFAF. The expansion coefficient of this study is based on 6, and a set of experiments are set every 2, and a total of 4 experiments are set. The expansion coefficient is divided into :rate1={1,2,4,8,10}, rate2={1,4,8,12,16}, rate3={1,6,12,18,24}, rate1={1,2,4,8, 12,16}, Rate3 ={1,6,12,18,24}, rate4= {1,8,16,24,32}. Based on the ResNet-18 network structure, we conducted MFA network optimization experiment and obtained the comparison results. Table 7 shows the experimental results of different expansion coefficients, and Figure 7 shows the effect analysis diagram of each expansion coefficient. It can be seen from Table 7 and Figure 7 that rate3 is the best expansion coefficient used in the ablation experiment in this paper. As can be seen from the rules of rate1, rate2 and rate3, the model's performance in all aspects (Accuracy, AUC, Recall and F1-Score) is improved with the increase of expansion coefficient. When the expansion coefficient reaches rate4, the Accuracy, AUC, Recall and F1-Score of our model are all reduced. This indicates that the larger the coefficient of expansion is not the better, and the most appropriate coefficient of expansion

Preprints (www.preprints.org) | NOT PEER-REVIEWED | Posted: 5 June 2023 doi:10.20944/preprints202306.0285.v1

should be selected to make the model better. In this paper, the expansion coefficient is set as rate3{1,6,12,18,24}.

**Figure 3.** Experimental Effect Diagram based on Expansion Coefficient.

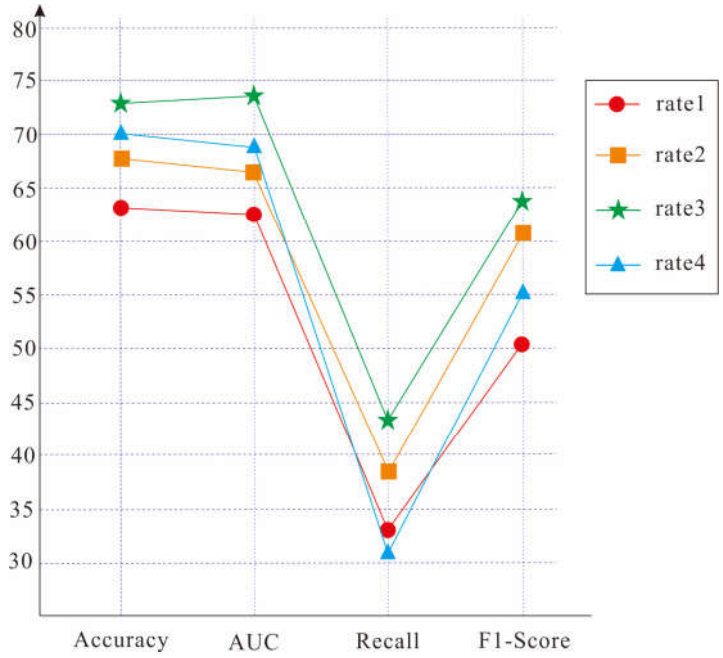


**Table 6**. Experimental Results based on Expansion Coefficient.

| Dilation rate | Accuracy | AUC | Recall | F1-Score |
|---|---|---|---|---|
| rate1 | 63.45 | 62.02 | 32.79 | 50.43 |
| rate2 | 67.34 | 66.22 | 38.28 | 61.14 |
| rate3 | 72.66 | 73.46 | 42.66 | 63.71 |
| rate4 | 70.22 | 68.86 | 31.46 | 55.65 |

*4.6. Visualization*

In this section, we use the MFAF trained in section 4.2 to predict the prospecting target area in the study area and visualize the prediction results. Specifically, 654 128×128×10 geo-image datasets were selected as input sources. Then, we use the trained MFA to predict and visualize it. Figure 8 shows the visualization result. Based on the visualization, we come to the following conclusions: (1) The predicted prospecting target area (No. 10, 19, 26, 49, 56, 58, 96, 123, 128) covers 100% of the known deposits and ore spots in the study area. (2) The predicted result area (No. 5, 9, 16, 28, 34, 41, 50, 72, 74, 75, 80, 97, 101, 124, 130) is different from the known deposit and ore spot location, it also has good metallogenic conditions and can be used as a deposit prediction area for further study. In summary, we can conclude that MFAF can fit the distribution of the prospecting target area in the Jinshan study area.

Preprints (www.preprints.org) | NOT PEER-REVIEWED | Posted: 5 June 2023 doi:10.20944/preprints202306.0285.v1

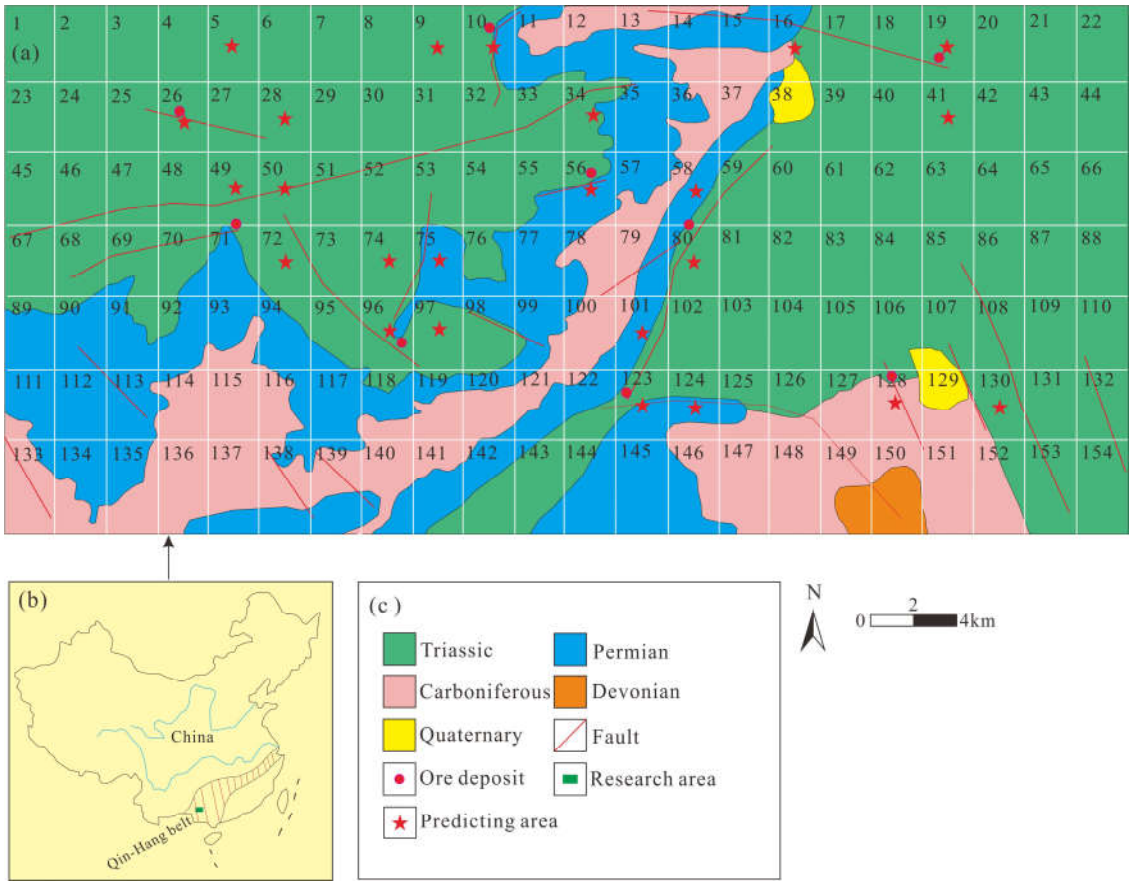


**Figure 4**. Prediction Diagram of Prospecting Target in the Study Area (a Geological diagram, b Location of the study area, c Legend).

## 5. Conclusions

In this paper, a deep learning (MFAF) for ore deposit identification and prediction is proposed based on the characteristics of geological data. And taking the Jinshan research area of Qin-hang metallogenic belt in China as the research object, the geological image data processing and ore deposit prediction are carried out. The results show that, compared with other research methods, the optimized model MFAF in this study is more suitable for intelligent identification and prediction of ore deposits in research area. Our model has obvious advantages in accuracy, AUC value and F1-Score, and the effect is better than other current mainstream deep learning models. The main conclusions of this paper are as follows:

1. The deep learning model of MFAF can effectively solve the problems of fine features of geological images and few mineral points in the region. In this model, expansion coefficient and multi-scale features are used to extract more and more detailed geological image feature information, and expansion convolution with different convolution kernel sizes is used to generate more labeled sample data.

2. The network architecture of channel attention and spatial attention mechanism was used to assign different weight coefficients to the geological image feature data of different channels and different spatial locations. It can avoid the influence of human subjective factors and improve the accuracy of intelligent identification and prediction of ore deposits based on geo-image data.

3. Smote method was used to enhance the labeled geological image samples. This can effectively expand the number of samples in geoscience image data set, ensure the data sent to the neural network to achieve balance, and complete the effective training of deep learning network model

4. In this study, MFAF was adopted to identify and predict the deposit in Jinshan research area. Experimental results showed that the predicted prospecting target area covered 100% of the known deposits in the study area. The other prediction areas have good metallogenic conditions and can be

 doi:10.20944/preprints202306.0285.v1

used as ore deposit prediction areas for further study. The research of this paper can provide resource guarantee and technical support for the sustainable exploitation of mineral resources and the sustainable growth of society and economy.

**Author Contributions:** Conceptualization, L.G. and K.W.; methodology, L.G.; software, X.Z.; validation, L.G., X.Z. and C.W.; formal analysis, L.G.; investigation, L.G.; resources, L.G.; data curation, C.W.; writing—original draft preparation, L.G.; writing—review and editing, K.W.; visualization, C.W.; supervision, L.G.; project administration, L.G.; funding acquisition, L.G. All authors have read and agreed to the published version of the manuscript.

**Institutional Review Board Statement:** Not applicable.

**Informed Consent Statement:** Not applicable.

**Data Availability Statement:** The data presented in this study are available on request from the corresponding author.

**Acknowledgments:** This work was supported by the Guangdong province teaching reform fund(No. GDJX2020009) and Bureau of Science and Technology of Jiangmen Municipality project(No. 2022JC01019).

**Conflicts of Interest:** The authors declare no conflict of interest.

## References

1. Cheng, Q. What are Mathematical Geosciences and its frontiers? Earth Science Frontiers. 2021, 28(3), 6-25. https://doi.org/10.13745/j.esf.sf.2021.1.17
2. Zhou, Y.; Zuo, R.; Liu, G.; Yuan, F.; Mao, X.; Guo, Y.; Xiao, F.; Liao, J.; Liu, Y. The Great-leap-forward Development of Mathematical Geoscience During 2010-2019: Big Data and Artificial Intelligence Algorithm Are Changing Mathematical Geoscience. Bulletin of Mineralogy, Petrology and Geochemistry. 2021, 40(3), 556-574. https://doi.org/10.19658/j.issn.1007-2802.2021.40.038
3. Zuo, R. Data science-based theory and method of quantitative prediction of mineral resources.Earth Science Frontiers. 2021, 28(3), 49-55. https://doi.org/10.13745/j.esf.sf.2020.12.1
4. Kost, S.; Rheinbach, O.; Schaeben, H. Using logistic regression model selection towards interpretable machine learning in mineral prospectivity modeling. Geochemistry. 2021, 81(4), 125826. https://doi.org/10.1016/j.chemer.2021.125826
5. Santos, J.S.; Ferreira, R.S.; Silva, V.T. Evaluating the classification of images from geoscience papers using small data. Applied Computing and Geosciences. 2020, 5, 1-7. https://doi.org/10.1016/j.acags.2019.100018
6. Ghezelbash, R.; Maghsoudi, A.; Carranza, E.J.M. Optimization of geochemical anomaly detection using a novel genetic K-means clustering (GKMC) algorithm. Computers & Geosciences. 2020, 134, 1-26. https://doi.org/10.1016/j.cageo.2019.104335
7. Martins, T.; Seoane, J..; Tavares, F. Cu-Au exploration target generation in the eastern carajas mineral province using random forest and multi-class index overlay mapping. Journal of South American Earth Sciences. 2022, 116. https://doi.org/10.1016/j.jsames.2022.103790
8. Li, T.; Zuo, R.; Zhao, X.; Zhao, K. Mapping prospectivity for regolith-hosted REE deposits via convolutional neural network with generative adversarial network augmented data. Ore Geology Reviews. 2022, 142, 104693. https://doi.org/10.1016/j.oregeorev.2022.104693
9. Zuo, R.; Carranza, E.J.M. Support vector machine: A tool for mapping mineral prospectivity. Computers & Geosciences, 2011, 37(12), 1967-1975. https://doi.org/10.1016/j.cageo.2010.09.014
10. Daviran, M.; Maghsoudi, A.; Ghezelbash, R.; Pradhan, B. A new strategy for spatial predictive mapping of mineral prospectivity: Automated hyperparameter tuning of random forest approach. Computers & Geosciences. 2021, 148, 104688. https://doi.org/10.1016/j.cageo.2021.104688
11. Chen, G.; Huang, N.; Wu, G.; Luo, L.; Wang, D.; Cheng, Q. Mineral prospectivity mapping based on wavelet neural network and Monte Carlo simulations in the Nanling W- Sn metallogenic province. Ore Geology Reviews. 2022, 143, 104765. https://doi.org/10.1016/j.oregeorev.2022.104765
12. Marjanovic, M.; Kovacevic, M.; Bajat, B.; Vozenilek, V. Landslide susceptibility assessment using SVM machine learning algorithm. Engineering Geology. 2011, 3, 225-234. https://doi.org/10.1016/j.enggeo.2011.09.006.
13. Zhang, C.; Zuo, R.; Xiong, Y.; Zhao, X.; Zhao, K. A geologically- constrained deep learning algorithm for recognizing geochemical anomalies. Computers & Geosciences. 2022, 162, 105100. https://doi.org/10.1016/j.cageo.2022.105100
14. Houshmand, N.; GoodFellow, S.; Esmaeili, K.; Calderon, J. Rock type classification based on petrophysical, geochemical, and core imaging data using machine and deep learning techniques. Applied computing and geosciences. 2022, 16, 100104. https://doi.org/10.1016/j.acags.2022.100104

15. Huang, Y.; Feng, Q.; Zhang, W.; Zhang, L.; Gao, L. Prediction of prospecting target based on selective transfer network. Minerals. 2022, 12, 1112. https://doi.org/10.3390/min12091112
16. Xiong, Y.; Zuo, R. Recognizing multivariate geochemical anomalies for mineral exploration by combining deep learning and one- class support vector machine. Computers & geosciences. 2020, 140, 104484. https://doi.org/10.1016/j.cageo.2020.104484
17. Gao, L.; Huang, Y.; Zhang, X.; Liu, Q.; Chen, Z. Prediction of prospecting target based on ResNet convolutional neural network. Applied sciences. 2022, 12, 11433. https://doi.org/10.3390/app122211433
18. Zhang, W.; Gu, X.; Tang, L.; Yin, Y.; Liu, D.; Zhang, Y. Application of machine learning, deep learning and optimization algorithms in geoengineering and geoscience: Comprehensive review and future challenge. Gondwana research. 2022, 109, 1-17. https://doi.org/10.1016/j.gr.2022.03.015
19. [19] Yang, F.; Li, N.; Xu, W.; Liu, X.; Cui, Z.; Jia, L.; Liu, Y.; Xu, J.; Chen, Y.; Xu, X.; Wang, J.; Qi, H.; Shu, R. Laser- induced breakdown spectroscopy combined with a convolutional neural network: a promising methodology for geochemical sample identification in Tianwen- 1 Mars mission. Spectrochimica acta part b: atomic spectroscopy. 2022, 192, 106417. https://doi.org/10.1016/j.sab.2022.106417
20. Li, Y.; Peng, C.; Ran, X.; Xue, L.; Chai, S. Soil geochemical prospecting prediction method based on deep convolutional neural networks- taking daqiao gold deposit in gansu province, China as an example. China geology. 2022, 5, 1, 71-83. https://doi.org/10.1016/S2096-5192(22)00087-8
21. Wang, Z.; Zuo, R. Mineral prospectivity mapping using a joint singularity- based weighting method and long short- term memory network. Computers & geosciences. 2022, 158, 104974. https://doi.org/10.1016/j.cageo.2021.104974
22. Zhang, C.; Zuo, R. Recognition of multivariate geochemical anomalies associated with mineralization using an improved generative adversarial network. Ore geology reviews. 2021, 136, 104264. https://doi.org/10.1016/j.oregeorev.2021.104264
23. Li, H.; Li, X.; Yuan, F.; Jowitt S.; Zhang, M.; Zhou, J.; Zhou, T.; Li, X.; Ge, C.; Wu, B. Convolutional neural network and transfer learning based mineral prospectivity modeling for geochemical exploration of Au mineralization within the Guandian- Zhangbaling area, anhui province, China. Applied geochemistry. 2020, 122, 104747. https://doi.org/10.1016/j.apgeochem.2020.104747
24. Chen, Y.; Shayilan, A. Dictionary learning for multivariate geochemical anomaly detection for mineral exploration targeting. Journal of geochemical exploration. 2022, 235, 106958. https://doi.org/10.1016/j.gexplo.2022.106958
25. He, Y.; Zhou, Y.; Wen, T.; Zhang, S.; Huang, F.; Zou, X.; Ma, X.; Zhu, Y. A review of machine learning in geochemistry and cosmochemistry: method improvements and applications. Applied geochemistry. 2022, 140, 105273. https://doi.org/10.1016/j.apgeochem.2022.105273
26. Huang, Y.; Gao, L.; Yang, T.; Zhang, X. Experimental research on intelligent prospecting based on multi-scale feature and meta- learning. Application research of computers. 2022, 39, 6, 1772-1778. https://doi.org/10.19734/j.issn.1001-3695.2021.10.0625
27. Dai, L.; Luo, M.; Zhang, T.; Huang, J.; Tang, Y.; Li, X.; Wu, F.; Nie, X. Method and practiceof rapid evaluation of soil thickness in low mountain and hilly area based on principal component analysis- taking luoshan county, henan province as an example. South china geology. 2021, 37, 4, 377-386. https://doi.org/10.3969/j.issn.2097-0013.2021.04.002
28. Peng, C.; Wang, L.; Jiang, D.; Yang, N.; Chen, R.; Dong, C. Establishing and validating a spotted tongue recognition and extraction model based on multiscale convolutional neural network. Digital Chinese Medicine. 2022, 5(1):49-58. https://doi.org/10.1016/j.dcmed.2022.03.005
29. Wang, Y.; Zhuang, Y.; Liu, Y.; Chen, B. MDISN: learning multiscale deformed implicit fields from single images. Visual informatics. 2022, 6, 2, 41-49. https://doi.org/10.1016/j.visinf.2022.03.003
30. Wen, C.; Wen, J.; Li, J.; Luo, Y.; Chen, M.; Xiao, Z.; Xu, Q.; Liang, X.; An, H. Lightweight silkworm recognition based on Multi- scale feature fusion. Computers and electronics in agriculture. 2022 200, 107234. https://doi.org/10.1016/j.compag.2022.107234
31. Chen, X.; Li, Y.; Nakatoh, Y. Pyramid attention object detection network with multi- scale feature fusion. Computers and electrical engineering. 2022, 104, 108436. https://doi.org/10.1016/j.compeleceng.2022.108436
32. Guan, Q.; Ren, S.; Chen, L.; Feng, B.; Yao, Y. A spatial- compositional feature fusion convolutional autoencoder for multivariate geochemical anomaly recognition. Computers & geosciences. 2021, 156, 104890. https://doi.org/10.1016/j.cageo.2021.104890
33. Zhou, W.; Yan, J.; Chen, C. Multiscale geophysics and mineral system detection: status and progress. Progress in geophysics. 2021, 36, 3, 1208-1225. https://doi.org/10.6038/pg2021EE0192
34. Li, K.; Zou, C.; Bu, S.; Liang, Y.; Zhang, J.; Gong, M. Multi-modal feature fusion for geographic image annotation. Pattern recognition. 2018, 73, 1-14. https://doi.org/10.1016/j.patcog.2017.06.036
35. Zhang, S.; Deng, X.; Lu, Y.; Hong, S.; Kong, Z.; Peng, Y.; Luo, Y. A channel attention based deep neural network for automatic metallic corrosion detection. Journal of building engineering. 2021, 42, 103046. https://doi.org/10.1016/j.jobe.2021.103046

36. Li, F.; Zhu, A.; Li, J.; Xu, Y.; Zhang, Y.; Yin, H.; Hua, G. Frequency-driven channel attention- augmented full-scale temporal modeling network for skeleton-based action recognition. Knowledge-based systems. 2022, 256, 109854. https://doi.org/10.1016/j.knosys.2022.109854
37. Wang, J.; Wu, X. A deep learning refinement strategy based on efficient channel attention for atrial fibrillation and atrial flutter signals identification. Applied soft computing. 2022, 130, 109552. https://doi.org/10.1016/j.asoc.2022.109552
38. Yu, G.; Luo, Y.; Deng, R. Automatic segmentation of golden pomfret based on fusion of multi- head self-attention and channel- attention mechanism. Computers and electronics in agriculture. 2022, 202, 107369. https://doi.org/10.1016/j.compag.2022.107369
39. Zhu, Y.; Gei, C.; So, E. Image super-resolution with dense-sampling residual channel-spatial attention networks for multi-temporal remote sensing image. International journal of applied earth observation and geoinformation. 2021, 104, 102543. https://doi.org/10.1016/j.jag.2021.102543
40. Gajbhiye, G.; Nandedkar, A. Generating the captions for remote sensing images: A spatial- channel attention based memory- guided transformer approach. Engineering applications of artificial intelligence. 2022, 114, 105076. https://doi.org/10.1016/j.engappai.2022.105076
41. Qiu, Z.; Becker, S.I.; Pegna, A.J. Spatial attention shifting to fearful faces depends on visual awareness in attentional blink: an ERP study. Neuropsychologia. 2022, 172, 108283. https://doi.org/10.1016/j.neuropsychologia.2022.108283
42. Kurki, I.; Hyvarinen, A.; Henriksson, L. Dynamics of retinotopic spatial attention revealed by multifocal MEG. Neuroimage. 2022, 263, 119643. https://doi.org/10.1016/j.neuroimage.2022.119643
43. Heo, J.; Wang, Y.; Park, J. Occlusion-aware spatial attention transformer for occluded object recognition. Pattern recognition letters. 2022, 159, 70-76. https://doi.org/110.1016/j.patrec.2022.05.006
44. Gendy, G.; Sabor, N.; Hou, J.; He, G. Balanced spatial feature distillation and pyramid attention network for lightweight image super-resolution. Neurocomputing. 2022, 509, 157-166. https://doi.org/10.1016/j.neucom.2022.08.053
45. Pan, D.; Xu, Z.; Lu, X.; Zhou, L.; Li, H. 3D scene and geological modeling using integrated multi-source spatial data: Methodology, challenges, and suggestions. Tunnelling and undergound space technology. 2020, 100, 103393. https://doi.org/10.1016/j.tust.2020.103393
46. Zhao, D.; Wang, X. Investigating the spatial distribution of antimony geochemical anomalies located in the Yunnan-Guizhou-Guangxi region, China. Geochemistry. 2021, 81, 4, 125829. https://doi.org/10.1016/j.chemer.2021.125829
47. Parisi, L.; Neagu, D.; Ma, R.; Campea, F. Quantum ReLu activation for convolutional neural networks to improve diagnosis of parkinson's disease and COVID-19. Expert systems with applications. 2022, 187, 115892. https://doi.org/10.1016/j.eswa.2021.115892
48. Zheng, Z.; Zhao, Q.; Li, S.; Qiu, S. Comparison of two machine learning algorithms for geochemical anomaly detection. Global Geology. 2018, 37(4), 1288-1294. https://doi.org/10.3969/j.issn.1004-5589.2018.04.030
49. Ozdemir, A.; Polat, K.; Alhudhaif, A. Classification of imbalanced hyperspectral images using SMOTE-based deep learning methods. Expert systems with applications. 2021, 178, 114986. https://doi.org/10.1016/j.eswa.2021.114986
50. Xie, Z.; Wang, Y.; Yu, M.; Yu, D.; Lv, J.; Yin, J.; Liu, J.; Wu, R. Triboelectric sensor for planetary gear fault diagnosis using data enhancement and CNN. Nano energy. 2022, 103, 107804. https://doi.org/10.1016/j.nanoen.2022.107804
51. He, K.; Zhang, X.; Ren, S.; Sun, J. Deep Residual Learning for Image Recognition. 2016 IEEE Conference on Computer Vision and Pattern Recogintion. 2016. https://doi.org/10.1109/cvpr.2016.90
52. Ma, N.; Zhang, X.; Zheng, H. Sun, J. ShuffleNet V2: Practical Guidelines for Efficient CNN Architecture Design. Lecture Notes in Computer Science. 2018, 122-138. https://doi.org/10.1007/978-3-030-01264-9_8
53. Hua, C.; Chen, S.; Xu, G.; Lu, Y.; Du, B. Defect identification method of carbon fiber sucker rod based on GoogLeNet-based deep learning model and transfer learning. Materialstoday communications. 2022, 33, 104228. https://doi.org/10.1016/j.mtcomm.2022.104228
54. Shafi, I.; Mazahir, A.; Fatima, A.; Ashraf, I. Internal defects detection and classification in hollow cylindrical surfaces using single shot detection and MobileNet. Measurement. 2022, 202, 111836. https://doi.org/10.1016/j.measurement.2022.111836
55. Tan, M.; Chen, B.; Pang, R.; Vasudevan, V.; Sandler, M.; Howard, A.; Le, Q. MnasNet: Platform-aware neural architecture search for mobile. Computer vision and pattern recognition 2019. 2019. https://doi.org/10.48550/arXiv.1807.11626
56. Tanveer, M.; Sharma, A.; Sugathan, P.N. General twin support vector machine with pinball loss function. Information sciences. 2019, 494, 311-327. https://doi.org/10.1016/j.ins.2019.04.032
57. Chu, C.; Ge, Y.; Qian, Q.; Hua, B.; Guo, J. A novel multi-scale convolution model based on multi-dilation rates and multi-attention mechanism for mechanical fault diagnosis. Digital signal processing. 2022, 122, 103355. https://doi.org/10.1016/j.dsp.2021.103355